# Enhanced Extrinsic Calibration Method for Camera-LiDAR Fusion and Monitoring of Safety Threats to Power Transmission Lines

Yulan Lao[1], Shuangfeng Wei[1,2], Guangzu Liu[3], Chuanyao Liu[1], Tong Yang[1]

[1] School of Geomatics and Urban Spatial Information, Beijing University of Civil Engineering and Architecture, Beijing 102616, China - 2108570023134@stu.bucea.edu.cn, weishuangfeng@bucea.edu.cn, 2108160222009@stu.bucea.edu.cn, 2108570022132@stu.bucea.edu.cn

[2] Engineering Research Center of Representative Building and Architectural Heritage Database, Ministry of Education, Beijing 102616, China - weishuangfeng@bucea.edu.cn

[3] The State Key Laboratory of Information Engineering in Surveying, Mapping and Remote Sensing, Wuhan University, Wuhan 430079, China - guangzu_liu@whu.edu.cn

**Keywords:** Power Transmission Line Collision Detection, Transmission Line Safety, Extrinsic Calibration, Distance Measurement

**Abstract**

Collision detection for ensuring safe navigation around power transmission lines is a critical task for maintaining operational safety. With advancements in sensor technology, cameras and LiDAR have been increasingly utilized for monitoring potential safety hazards associated with power lines. However, a single, fixed-position sensor may be insufficient to capture adequate information for accurately estimating the spatial relationship between transmission lines and mechanical equipment. To address this limitation, this paper proposes a method for measuring the spatial distance between transmission lines and mechanical equipment based on the simultaneous estimation of the relative position and orientation (extrinsic calibration) of the camera-LiDAR system. First, an enhanced extrinsic calibration technique for the camera-LiDAR system is introduced to effectively mitigate the impact of data noise on calibration results. Then, based on the calibration results, a spatial distance measurement method is developed to achieve more accurate distance calculations. Experimental evaluations using real-world data across various scenarios demonstrate that the proposed method exhibits strong robustness and accuracy, making it highly valuable for power transmission line safety monitoring and risk assessment.

## 1. Introduction

Transmission lines are essential for ensuring the continuity of electricity supply. However, improper operation of construction machinery can increase the risk of collisions with transmission lines. To prevent accidents, devices such as cameras and LiDAR have been increasingly employed for transmission line safety inspection. Traditional manual measurement methods are limited by low accuracy and efficiency. In response to these limitations, researchers have developed a combined LiDAR system that integrates airborne LiDAR and terrestrial laser scanners for transmission line measurement (Lin et al., 2023). Furthermore, to account for environmental factors such as wind-induced displacement, some studies have developed methods for transmission line modeling based on LiDAR point cloud reconstruction to enhance measurement accuracy (Ma et al., 2023). In contrast to the constraints of single-sensor systems, the integration of cameras and LiDAR provides both rich color and texture information as well as precise spatial data (Xiong et al., 2024), offering more comprehensive support for transmission line collision detection. The extrinsic calibration of LiDAR and cameras is fundamental to joint measurement, as it is performed to determine the relative position and orientation of sensors in three-dimensional space, thereby establishing an accurate correspondence between point clouds and images.

Extrinsic calibration methods for LiDAR-camera systems are generally classified into two main types: targetless calibration and target-based calibration. Targetless methods eliminate the need for manually placed calibration targets and typically include feature-based calibration and motion-based calibration (Xiao et al., 2021). Feature-based methods utilize structural features present in the environment. For instance, the Hough Transform can be used to extract linear features from a calibration board, and the extrinsic parameters can then be estimated by enforcing constraints on the relationship between point cloud normal vectors and image normal vectors (Qin et al., 2022). Additionally, common linear features can be extracted from both camera images and point clouds, which are subsequently optimized using a 2D-3D line feature error minimization approach (Moghadam et al., 2013). The fundamental principle of these methods is to establish correspondences between 2D and 3D features in the environment, formulate constraint equations, and solve for the extrinsic parameters through optimization. However, these methods often require human intervention in high-noise scenarios. To enhance computational efficiency, Vasconcelos et al. (2012) proposed a minimal solver, which can accurately determine extrinsic parameters with a limited number of data samples. Nevertheless, this method lacks robustness in high-noise environments and requires additional optimization strategies to improve stability. Motion-based methods treat LiDAR-camera calibration as a hand-eye calibration problem (Shiu et al., 1989), which estimates calibration parameters by analyzing sensor motion sequences (Strobl et al., 2006). Huang et al. (2017) employed the Gauss-Helmert error model to address motion constraints while simultaneously optimizing both sensor-relative motion and extrinsic parameters. To further improve computational efficiency, Unnikrishnan and Hebert (2005) proposed a fast extrinsic calibration method, which significantly decreases computational overhead and enhances real-time performance, making it suitable for large-scale data processing and dynamic environments. However, these methods impose strict requirements on the sensor's motion trajectory; if the trajectory is overly simplistic or inconsistent, it may adversely affect the accuracy of extrinsic parameter estimation.

Compared to target-free calibration methods, target-based calibration methods offer advantages such as improved robustness and enhanced accuracy. These methods determine the relative positions between sensors based on the spatial poses of calibration targets in their respective sensor coordinate systems. Zhang, (2000) first introduced the use of a 2D checkerboard calibration board, laying the foundation for camera calibration. However, this approach is limited to 2D planes and fails to account for point correspondences in 3D space, thereby restricting its applicability. To overcome this limitation, Zhang and Pless (2004) proposed an extrinsic calibration method based on multi-plane constraints, which can handle point correspondences in 3D space, thereby broadening the applicability of calibration methods. This method is not confined to a single planar structure and is suitable for more complex three-dimensional environments. However, it still relies on the precise placement of the calibration board, reducing its effectiveness in dynamic environments. To further enhance calibration flexibility, Tsai et al. (1987) introduced the Variability of Quality (VOQ) metric based on the checkerboard calibration method. By assigning scores to each calibration sample, this approach improved the overall accuracy of calibration. Additionally, other studies have explored the use of arbitrarily shaped tetrahedrons (Tian et al., 2020), multiple sets of polygonal calibration boards (Part et al., 2014), and even cardboard boxes (Pusztai et al., 2017) as calibration targets to reduce calibration costs.

Although the aforementioned methods have improved calibration accuracy to varying degrees, challenges remain regarding adaptability to varying environments and the level of automation. In recent years, deep learning has been increasingly applied to the calibration of LiDAR-camera systems. Tan et al. (2024) conducted a systematic review of deep learning-based extrinsic calibration methods, emphasizing that neural networks facilitate automatic feature extraction, which enhances the robustness and adaptability of the calibration process. Compared to traditional approaches, deep learning methods enable calibration with fewer or even no physical targets, significantly reducing the need for manual intervention. However, these methods are highly dependent on training data, and their generalization ability remains a key challenge.

To address the limitation of a single sensor in accurately recognizing and measuring the spatial distance between power transmission lines and mechanical equipment, this study proposes a refined extrinsic calibration approach for camera-LiDAR integration and applies it to the measurement of distances between power lines and machinery. The proposed approach reduces the influence of complex construction environments on distance estimation accuracy, making it highly significant for the safety assessment and predictive maintenance of power transmission lines.

## 2. Methodology

Initially, in the camera intrinsic calibration stage, Zhang's method is employed to obtain the homography matrix. Based on the relationship between the camera's intrinsic parameters and the homography matrix, the intrinsic parameter matrix $K_{int}$ is derived by decomposing the homography matrix and computing its inverse.In the extrinsic calibration stage, the Perspective-n-Point (PnP) problem (Moreno-Noguer et al., 2007) is solved, where the extrinsic parameter matrix $K_{ext}$ is estimated using the camera's intrinsic parameters, 3D point cloud coordinates, and corresponding 2D projection points in the image. This method employs the Efficient Perspective-n-Point (EPnP) algorithm (Lepetit et al., 2009) to obtain an initial estimate of the extrinsic parameters, which is then refined using the Levenberg-Marquardt (L-M) algorithm (Hartley et al., 2003), ultimately producing a robust optimal solution.

The extrinsic calibration algorithm in this method integrates Zhang's calibration technique with the optimized EPnP algorithm for estimating extrinsic parameters. The main framework is illustrated in Figure 1, with a primary focus on the extrinsic calibration process.

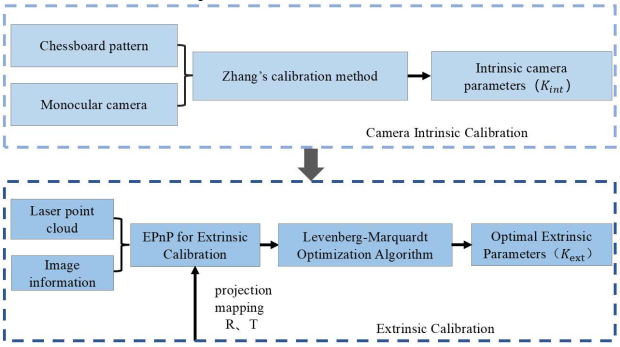


Figure 1. Flowchart of the LiDAR and camera extrinsic calibration process.

### 2.1 Camera Intrinsic Parameter Estimation

Within the camera imaging model, the intrinsic matrix characterizes the internal optical properties of the camera. It maps 3D points from the camera coordinate system to the image plane, thereby determining the corresponding pixel positions in the image. This study employs the world coordinate system, the camera coordinate system, and the image coordinate system to describe the camera imaging model based on the pinhole imaging principle, as illustrated in Figure 2. Here, $O_w X_W Y_w Z_w$ represents the world coordinate system, $O_C X_C Y_C Z_C$ denotes the camera coordinate system, and $(u, v)$ is the image pixel corresponding to the spatial point $P(X, Y, Z)$ after transformation via the camera projection model.

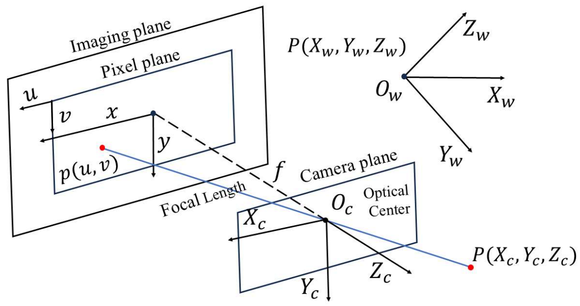


Figure 2. The pinhole imaging model of the camera.

Based on the principles of camera imaging, a transformation model that converts 3D world coordinates into 2D image coordinates while accounting for lens distortion is established. The specific transformation formula is provided in equation (1):

$$\begin{bmatrix} u_d \\ v_d \\ 1 \end{bmatrix} = \begin{bmatrix} \frac{f}{d_x} & 0 & c_x & 0 \\ 0 & \frac{f}{d_y} & c_y & 0 \\ 0 & 0 & 1 & 0 \end{bmatrix} \begin{bmatrix} R & T \\ 0^T & 1 \end{bmatrix} \begin{bmatrix} X_W \\ Y_W \\ Z_W \\ 1 \end{bmatrix} = K_{int} K_{ext} \begin{bmatrix} X_W \\ Y_W \\ Z_W \\ 1 \end{bmatrix} \quad (1)$$

where $u_d$ , $v_d$ = image pixel coordinates after distortion correction.
$f$ = camera's focal length

$d_x, d_y$ = physical lengths of a single pixel along the x and y axes
$c_x, c_y$= offset of the projection screen's center relative to the optical axis
$T$ = translation matrix
$R$ = rotation orthogonal matrix
$K_{int}$ = camera's internal parameter matrix
$K_{ext}$ = camera's external parameter matrix

Subsequently, Brown's distortion model is applied, with the specific transformation formula given in equation (2):

$$\begin{bmatrix} u \\ v \\ 1 \end{bmatrix} = \begin{bmatrix} 1+k_1r^2+k_2r^4+k_3r^6 & 2p_1xy+p_2(r^2+2x^2) & 0 \\ 2p_2xy+p_1(r^2+2y^2) & 1+k_1r^2+k_2r^4+k_3r^6 & 0 \\ 0 & 0 & 1 \end{bmatrix} \begin{bmatrix} u_d \\ v_d \\ 1 \end{bmatrix} \quad (2)$$

where $u$,$v$= actual image pixel coordinates
$r^2$ = sum of squares of the image coordinates after distortion correction
$x$, $y$= offset of the image coordinates after distortion correction relative to the principal point
$k_1$, $k_2$, $k_3$= radial distortion coefficients
$p_1$, $p_2$= tangential distortion coefficients

When at least three calibration images are available, the 2D image points and their corresponding 3D point cloud points yield a system of equations that form an overdetermined system. While a minimum of six point correspondences is required, increasing the number of points typically necessitates a nonlinear optimization method, such as least squares, to accurately estimate the intrinsic matrix $K_{int}$.

In this study, we employ Zhang's calibration method for monocular camera calibration. While, in theory, three images are sufficient to determine the camera's intrinsic parameters, we captured 20 images to ensure numerical stability, a high signal-to-noise ratio, and improved calibration accuracy. The process of detecting corner points in the images is illustrated in Figure 3.

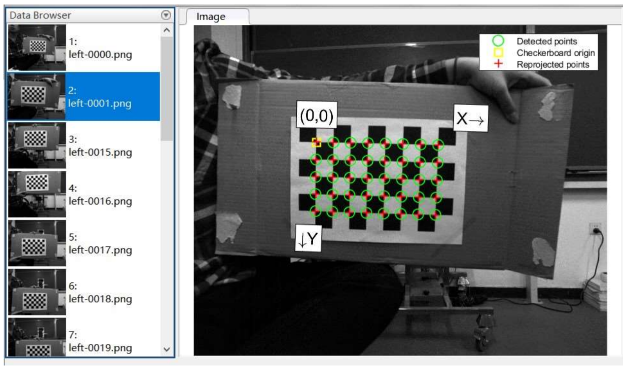


Figure 3. Schematic diagram of the image corner point detection.

Using the corner point data extracted from these 20 frames, the internal parameters of the camera were computed. The calibration results are summarized in Table 1.

| Internal Parameters | Calibration Results |
|---|---|
| Focal Length (pixel) | $f_x/d_x$=836.5595, $f_y/d_y$=837.5927 |
| Principal Point (pixel) | $c_x$=632.6342, $c_y$=518.6429 |
| Radial Distortion | $k_1 = -0.0915$, $k_2 = 0.04930$, $k_3 = 0.02400$ |
| Tangential Distortion | $p_1 = -0.00015572$, $p_2 = 0.000004930$ |

Table 1. Calibration results of camera intrinsic parameters

The calibration errors of the intrinsic parameters are illustrated in Figure 4, with the overall mean reprojection error remaining below 0.19 pixels, which adequately meets the requirements for practical engineering applications.

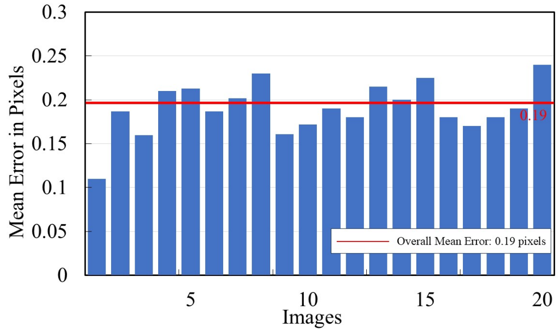


Figure 4. Average reprojection error of corner points

The accuracy and reliability of the extrinsic calibration results were assessed by calculating the differences between the observed and projected pixel coordinates, known as the reprojection error. The error for each point is denoted as $ei$, where $i$ is the index of the point within the dataset. To ensure all points are accounted for, the total reprojection error is obtained by summing the individual errors over all points, as expressed in equation (3):

$$E = \sum_{i=1}^{n} \left\| P_{proj,i} - P_{obs,i} \right\| \quad (3)$$

where $P_{proj,i}$ = projected pixel coordinates for the i-th point
$P_{obs,i}$ = observed pixel coordinates for the i-th point
n = total number of points

### 2.2 Extrinsic Calibration Algorithm Optimization

The extrinsic calibration between the LiDAR sensor and the camera involves determining the spatial relationship between the two devices, as depicted in Figure 5. This is achieved by establishing a transformation matrix that relates each pixel in the 2D image to the corresponding points on the surface of objects in space, thereby aligning RGB images with 3D point clouds within a unified coordinate system. This facilitates the fusion and spatial synchronization of multi-sensor data. The core challenge in estimating the extrinsic parameters lies in addressing the PnP problem. The EPnP method provides an effective solution, renowned for its computational efficiency and fast processing speed.

The EPnP method represents the coordinates of each 3D reference point as a linear combination of four non-coplanar control points. The mathematical formulation for expressing the coordinates of reference points in terms of control points is given as follows:

$$p_i^w = \sum_{j=1}^{4} \alpha_{ij} c_j^w \text{, with} \sum_{j=1}^{4} \alpha_{ij} = 1 \quad (4)$$

where $p_i^w$ = coordinates of the 3D reference point in the world coordinate system
$c_j^w$ = corresponding control point coordinates
$\alpha_{ij}$ = homogeneous barycentric coordinates

Similarly, in the camera coordinate system, each 3D reference point is expressed using the same linear combination:

$$p_i^c = \sum_{j=1}^{4} \alpha_{ij} c_j^c \,, with \sum_{j=1}^{4} \alpha_{ij} = 1 \tag{5}$$

where $p_i^c$ = coordinates of the 3D reference point in the camera coordinate system
$c_j^c$ = corresponding control point coordinates
$\alpha_{ij}$ = homogeneous barycentric coordinates

The extrinsic parameters are determined using the Iterative Closest Point (ICP) method (Besl et al., 1992). Since the EPnP algorithm is sensitive to noise and outliers in the input data during camera pose estimation and strongly depends on the initial extrinsic parameters, an improper selection of initial values may lead to local optima. The Levenberg-Marquardt (L-M) algorithm combines the rapid convergence of the Gauss-Newton method with the stability of gradient descent, which adaptively adjusts the damping factor to avoid local minima. Therefore, the proposed approach employs the L-M algorithm for optimization, specifically by using the extrinsic parameters estimated by the EPnP algorithm as the initial solution and setting the sum of squared residuals as the objective function, as shown in equation (6):

$$f(R) = \sum_{i}^{n} \rho(\|p_i^c - \pi(K_{int}, R_{rot}, T, p_i^w)\|^2) \tag{6}$$

where $R$ = extrinsic parameter vector
$\pi$ = camera's projection function
$K_{int}$ = camera's intrinsic matrix
$R_{rot}, T$ = rotation and translation matrices
$\rho$ = robust kernel function used to handle outliers

With each iteration, the extrinsic parameters $R$ are updated to minimize the objective function, as expressed in equation (7):

$$R_{new} = R_{old} - (\mathcal{J}^T \mathcal{J} + \lambda \mathcal{D})^{-1} \mathcal{J}^T r \tag{7}$$

where $\mathcal{J}$ = Jacobian matrix
$r$ = residual vector
$\lambda$ = damping factor
$\mathcal{D}$ = diagonal matrix

Through the iterative optimization process, the reprojection error is progressively minimized, yielding more accurate estimates of the extrinsic parameters. This not only enhances the robustness of the algorithm but also ensures a gradual convergence toward the optimal solution.

## 3. Experiments and Results

### 3.1 Experimental Equipment

In this study, the experimental setup employs the DJI Livox Avia LiDAR and the FLIR Blackfly BFS-U3-13Y3C-C camera as sensors, where the Intel NUC functions as the computational platform for constructing the hardware system, as illustrated in Figure 5. The hardware specifications are summarized in Table 2.

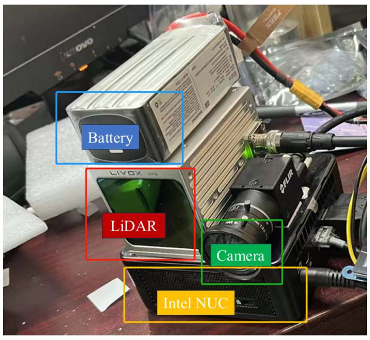


Figure 5. Hardware system platform

| Hardware | Model | Parameter |
|---|---|---|
| LiDAR | Livox Avia | FOV: 70.4° × 77.2° |
| Camera | LIR Blackfly BFS-U3-13Y3C-C | FOV: 82.9° × 66.5° |
| Computing Platform | Intel NUC | CPU: Intel i5-1135G7 Memory: 32G |

Table 2. Specific parameters of the hardware system platform configuration

### 3.2 Results and Analysis

To ensure the efficacy and reliability of the algorithm in practical applications, this study adopts a phased experimental validation approach. Initially, indoor and outdoor environments of the school's laboratory building were selected for preliminary experiments. This approach aimed to verify the fundamental performance and stability of the algorithm within a relatively controlled environment.

Acknowledging that factors such as lighting and distance could potentially influence the sensors, the experimental setup was used to acquire point cloud data and images from indoor and outdoor scenes at the school's laboratory building, as illustrated in Figure 6.

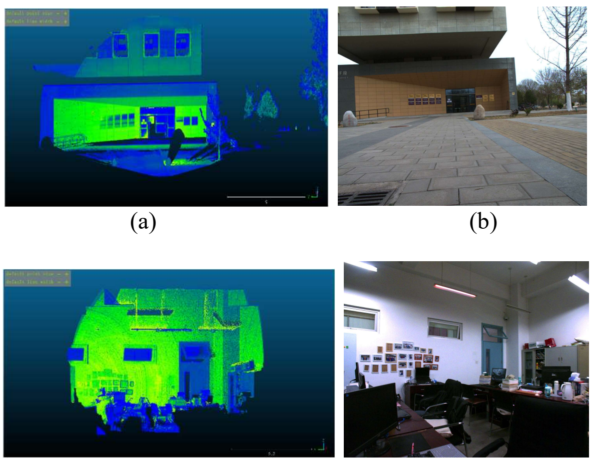

(a) (b) (c) (d)

Figure 6. Point cloud data and corresponding images. (a), (b) Outdoor scene; (c), (d) Indoor scene.

For both indoor and outdoor scenes, four non-collinear feature points from the point cloud and their corresponding image projection points were selected. A comparative analysis was performed using the traditional EPnP algorithm in comparison with the EPnP+L-M algorithm introduced in this study. The reconstructed pixel coordinates were compared with the actual pixel coordinates, and the error statistics are summarized in Tables 3 and 4.

| Calibration algorithm | Actual 2D pixel coordinates | | Estimated pixel coordinates | | Reprojection error |
|---|---|---|---|---|---|
| EpnP | 467 | 491 | 465.5373 | 488.7321 | 2.6986 |
| | 596 | 341 | 596.0272 | 340.8274 | 0.1746 |
| | 831 | 341 | 829.3659 | 340.6119 | 1.6795 |
| | 448 | 318 | 452.0792 | 321.0099 | 5.0695 |
| | Average reprojection error | | | | **2.4055** |
| Ours | 467 | 491 | 467.0088 | 490.9886 | 0.0143 |
| | 596 | 341 | 596.1834 | 340.3190 | 0.7052 |
| | 831 | 341 | 830.9501 | 341.2738 | 0.2783 |
| | 448 | 318 | 447.8622 | 318.4196 | 0.4417 |
| | Average reprojection error | | | | **0.3599** |

Table 3. Statistical analysis of coordinate reconstruction errors for indoor scenes.

| Calibration algorithm | Actual 2D pixel coordinates | | Estimated pixel coordinates | | Reprojection error |
|---|---|---|---|---|---|
| EpnP | 836 | 409 | 836.0375 | 409.0204 | 0.04271 |
| | 704 | 419 | 704.3165 | 418.9449 | 0.3213 |
| | 869 | 124 | 868.9937 | 124.0043 | 0.0075 |
| | 554 | 426 | 553.6462 | 426.0342 | 0.3554 |
| | Average reprojection error | | | | **0.1817** |
| Ours | 836 | 409 | 835.8644 | 409.0399 | 0.1413 |
| | 704 | 419 | 704.3367 | 418.9436 | 0.3414 |
| | 869 | 124 | 868.9795 | 124.0075 | 0.0218 |
| | 554 | 426 | 553.8269 | 426.0060 | 0.1731 |
| | Average reprojection error | | | | **0.1694** |

Table 4. Statistical analysis of coordinate reconstruction errors for outdoor scenes.

Tables 3 and 4 present the reprojection errors of the two algorithms in indoor and outdoor scenes, respectively. A comparison of the data in these tables reveals that the calibration algorithm employed in this study demonstrates a substantial improvement over the traditional EPnP algorithm in terms of accuracy, especially in indoor calibration scenarios. The EPnP algorithm exhibits an average reprojection error of 2.4 pixels, whereas the proposed algorithm achieves a significantly lower error of 0.35 pixels.

To account for the uncertainties and noise inherent in real-world conditions, this research introduces zero-mean Gaussian noise with a variance of 4 to the image pixel coordinates of the control points, thus simulating real-world conditions where accurately extracting control point pixel coordinates from images is difficult.

This study validates the effectiveness of the proposed method by comparing errors in Euler angles, translation, and reprojection. Figures 7 and 8 illustrate the error curves for images with a noise variance of 4 in both indoor and outdoor scenes. Specifically, Figures 7(a) and 8(a) display the pose estimation error curves, while Figures 7(b) and 8(b) present the translation estimation error curves. Figure 9 illustrates the reprojection error curves for both indoor and outdoor scenes under the same noise variance. As shown in the figures, as the image noise level increases, the pose estimation results of the EPnP algorithm become unstable. In contrast, the proposed EPnP+L-M algorithm exhibits strong stability and robustness even in the presence of significant noise and uncertainty. These results establish a reliable basis for applications in complex construction environments.

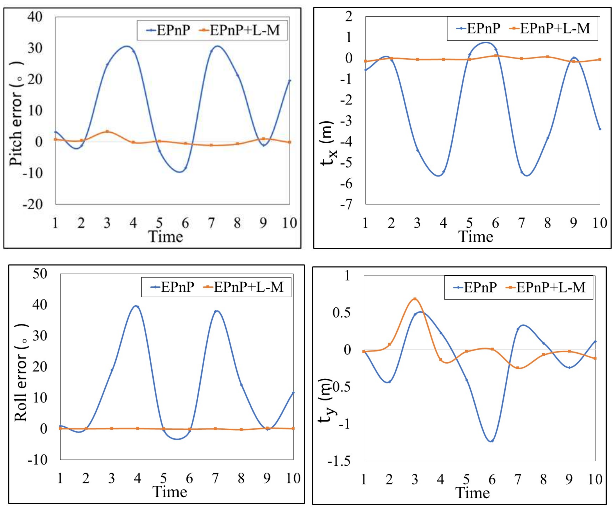

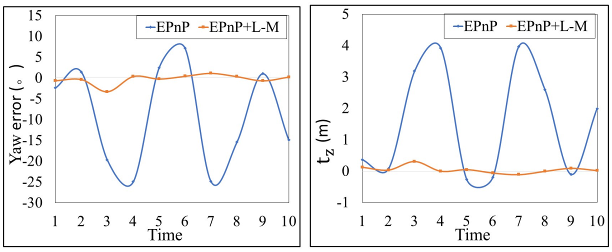


(a) (b)

Figure 7． Curves for indoor scene images with a noise variance of 4. (a) Pose estimation curve; (b) Displacement estimation curve.

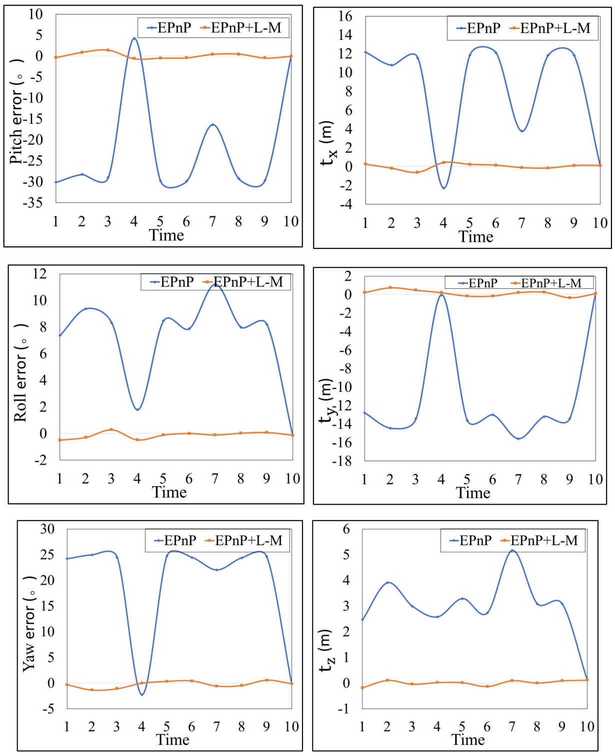


(a) (b)

Figure 8． Curves for outdoor scene images with a noise variance of 4. (a) Pose estimation curve; (b) Displacement estimation curve.

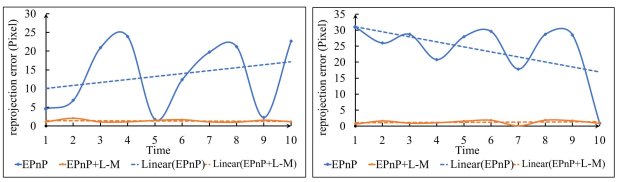


(a) (b)

Figure 9: Reprojection error with a noise variance of 4. (a) Reprojection error for the indoor scene; (b) Reprojection error for the outdoor scene.

By conducting experimental analyses of point cloud data and images in both indoor and outdoor campus environments, the superior accuracy and robustness of the proposed algorithm can be evaluated under relatively simple conditions, thus laying a solid foundation for further experimentation. The algorithm was subsequently applied to a more complex real-world transmission line environment, where it was used to measure the distance between mechanical equipment and power lines.

Three sets of construction machinery scenes at varying distances were selected, including both close-range and long-range scenarios, to verify the effectiveness of the proposed method. Each scene represents a range of exposure conditions, including normal exposure (NE) and overexposure (OE), as shown in Table 5, to simulate potential lighting challenges encountered in real-world imaging.

In this study, our primary objective was to segment the transmission lines in proximity to the construction machinery from the scene's point cloud. Subsequently, an Oriented Bounding Box (OBB) was constructed around the transmission lines. By applying three-dimensional geometric principles, the coordinates of the eight vertices of this bounding box were computed, which served as the basis for subsequent distance calculations. The algorithm presented in this study was subsequently employed to calculate the corresponding three-dimensional coordinates of the two-dimensional pixel bounding box and determine the depth value representing the distance between the construction machinery and the transmission line. To validate the accuracy, the shortest distance between the machinery and the transmission line was measured using Cloud Compare software (Daniel Girardeau-Montaut, 2024), with this measurement serving as the reference for the true value, as shown in Table 6. A comparison between the computed distance and the true shortest distance allows for an assessment of the algorithm's effectiveness in practical applications.

| Scene | Normal Exposure | Overexposure |
|---|---|---|
| Scene 1 |  | 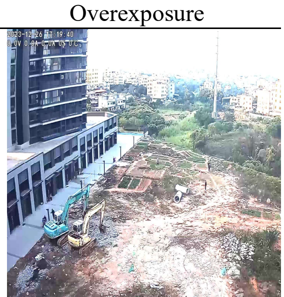 |
| Scene 2 |  |  |
| Scene 3 | 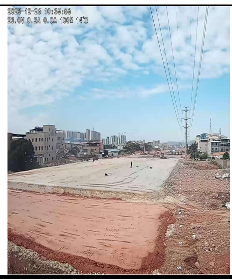 |  |

Table 5. Scene images under different exposures.

| Scene | Point cloud of scene | True distance(m) |
|---|---|---|
| Sene 1 | 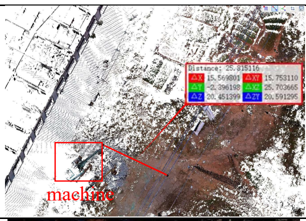  | 25.815 |
| Scene 2 | 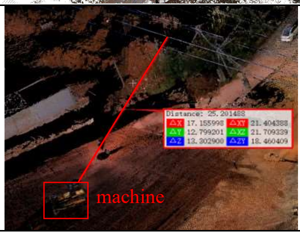  | 25.201 |
| Scene 3 | 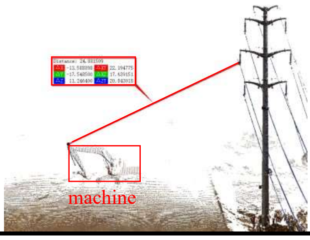  | 24.881 |

Table 6. The true distance between the machinery and the transmission lines in three scenarios.

Table 7 presents the results of the distance calculations between construction machinery and transmission lines, together with error evaluations under two distinct exposure conditions. The proposed algorithm demonstrated high accuracy and robustness across all scenarios. The absolute error remained within 2 meter, and the relative error was consistently below 10%, even under the demanding conditions of normal and overexposure. This level of precision meets the safety distance standards that must be maintained between construction machinery and transmission lines; therefore, it is critical for the maintenance and safety monitoring of power transmission lines.

| Scene | Our Method(m) | | Error(m) | Relative Error(%) |
|---|---|---|---|---|
| Scene 1 | NE | 24.512 | 1.303 | 5.047 |
| | OE | 24.294 | 1.521 | 5.892 |
| Scene 2 | NE | 23.596 | 1.605 | 6.368 |
| | OE | 23.589 | 1.612 | 6.396 |
| Scene 3 | NE | 23.046 | 1.835 | 7.375 |
| | OE | 23.039 | 1.842 | 7.403 |

Table 7. The results of the distance calculations between construction machinery and transmission lines

## 4. Conclusions

This study presents an enhanced extrinsic calibration method, applied to calculate the spatial distance between transmission lines and construction machinery. In the context of power line safety operations, maintaining a safe distance between transmission lines and surrounding machinery is critical. To assess the basic performance and stability of the algorithm in a controlled environment, we employed a phased experimental validation approach, conducting tests in both low-complexity campus scenarios and real-world construction settings. The results demonstrate that the optimized extrinsic calibration algorithm yields minimal reprojection errors and delivers stable results, even under noisy conditions. Furthermore, it provides accurate assessments when determining the shortest distance between transmission lines and construction machinery. Overall, the algorithm demonstrates robust performance in determining extrinsic parameters in complex construction environments.

In future work, we plan to further refine the algorithm presented in this study. Future research may combine automatic feature extraction algorithms with manual selection to reduce feature corner mismatches and enhance calibration accuracy. The ultimate goal is to achieve more precise monitoring of construction site safety.

## References

Besl, P. J., McKay, N. D., 1992. A Method for Registration of 3-D Shapes. *IEEE Transactions on Pattern Analysis and Machine Intelligence*, 14(2), 239-256.

Daniel Girardeau-Montaut, 2024. CloudCompare Software, Version 2.13.0. http://www.cloudcompare.org (14 February 2024).

Huang, K., Stachniss, C., 2017. Extrinsic Multi-sensor Calibration for Mobile Robots Using the Gauss Helmert Model. *IEEE International Conference on Intelligent Robots and Systems*, 1-8.

Hartley, R., Zisserman, A., 2003. Multiple view geometry in computer vision. *Cambridge university press.*

Lin, Y., Li, B., Bai, Z., 2023. Application of combined LiDAR system in power line measurement. *Electrical Measurement and Instrumentation*, 60(02), 32-36.

Lepetit, V., Moreno-Noguer, F., Fua, P., 2009. EPnP: An Accurate O(n) Solution to the PnP Problem. *Int J Comput Vis* 81, 155-166.

Ma, W., Wang, C., Wu, X., 2023. Airborne Laser Point Cloud Power Line Model Reconstruction Considering Wind Bias. *Remote Sensing Information*, 38(02), 56-63.

Moghadam, P., Bosse, M., Zlot, R., 2013. Line-based extrinsic calibration of range and image sensors. *IEEE International Conference on Robotics and Automation*, 3685- 3691.

Moreno-Noguer, F., Muñoz, D., Torr, P. H. S., 2007. Accurate non-iterative O(n) solution to the PnP Problem. *IEEE International Conference on Computer Vision (ICCV)*, 2007, 1–8.

Pandey, G., McBride, J., Savarese, S., 2015. Automatic Extrinsic Calibration of Vision and LiDAR by Maximizing Mutual Information. *Journal of Field Robotics*, 32(5), 696-722.

Park, Y., Yun, S., Won, C., 2014. Calibration between color camera and 3D LIDAR instruments with a polygonal planar board. *Sensors*, 14(3), 5333-5353.

Pusztai, Z., Hajder, L., 2017. Accurate calibration of LiDAR-camera systems using ordinary boxes. *IEEE International Conference on Computer Vision Workshops*, 394-402.

Qin, X., Li, X., Tang, X., 2022. Calibration Method for the Extrinsic Parameters of LiDAR and Camera Based on Key Points of Calibration Board. *Advances in Laser and Optoelectronics*, 59(4), 400-407.

Shiu, Y., Ahmad, S., 1989. Calibration of wrist-mounted robotic sensors by solving homogeneous transform equations of the form AX=XB. *IEEE Transactions on Robotics*, 5(1), 16-29.

Strobl, K., Hirzinger, G., 2006. Optimal hand-eye calibration. *IEEE/RSJ International Conference on Intelligent Robots and Systems*, 1-8.

Tian Z., Huang Y., Zhu F., 2020. The extrinsic calibra- tion of area scan camera and 2D laser range finder (LRF) using checkerboard trihedron. *IEEE Access*, 321(8), 36166-36179.

Tsai, R., 1987. A Versatile Camera Calibration Technique for High-accuracy 3D Machine Vision Metrology Using Off-the-shelf TV Camera and Lenses. *IEEE Journal on Robotics and Automation*, 3(4), 323-344.

Tan, J., Liu, X., Chen, Y., Wang, H., Wu, Y., 2024. A Review of Deep Learning-Based LiDAR and Camera Extrinsic Calibration. *Sensors*, 24(1), 1-25.

Unnikrishnan, R., Hebert, M., 2005. Fast Extrinsic Calibration of a Laser Rangefinder to a Camera. *Technical Report CMU-RI-TR-05-09, Carnegie Mellon University.*

Vasconcelos, F., Barreto, J. P., Nunes, U., 2012. A Minimal Solution for the Extrinsic Calibration of a Camera and a Laser-Rangefinder. *IEEE Transactions on Pattern Analysis and Machine Intelligence*, 34(11), 2097-2107.

Xiong, C., Wu, M., Liu, Z., 2024. Research on the Progress of Lidar and Camera Joint Calibration. *Journal of Navigation and Positioning*, 12(02), 155-166.

Xiao, J., Shi, C., Huang, K., 2021. Extrinsic Calibration and Fusion Odometry Study of Monocular Camera and 3D LiDAR. *Robotics*, 43(01), 17-28.

Zhang, Z., 2000. A Flexible New Technique for Camera Calibration. *IEEE Transactions on Pattern Analysis and Machine Intelligence*, 22(11), 1330–1334.

Zhang, Q., Pless, R., 2004. Extrinsic calibration of a camera and laser range finder. *IEEE/RSJ International Conference on Intelligent Robots and Systems (IROS)*, 2004.